1.1 Modeling, Analysis, and Simulation of All-semiconductor Photonic-crystal Surface-emitting Lasers

Mindaugas Radziunas and Eduard Kuhn

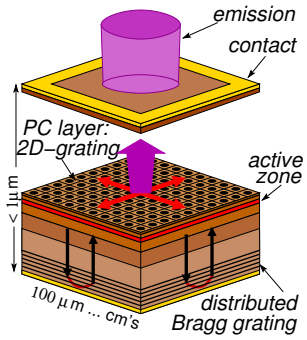

Fig. 1: *Schematics of photonic-crystal surface-emitting semiconductor laser*

Semiconductor lasers (SLs) are compact, efficient, durable, and cost-effective devices used in various modern applications. Among these, material processing often demands optical power up to several kilowatts. High-power edge-emitting SLs, commonly used for such purposes, face challenges like large asymmetric beam divergence and poor lateral beam quality due to multiple lateral optical modes contributing to laser emission. In 1999, Prof. Susumu Noda (Kyoto University) proposed the Photonic-Crystal (PC) surface-emitting laser (SEL), shown schematically in Figure 1. These SLs consist of multiple thin layers, most of which are uniform in two lateral directions. The vertical structure ensures the selection of a single vertical transverse-electric optical mode. Near the active zone, a PC layer induces a two-dimensional (2D) band-edge resonant effect, enabling both light amplification and surface emission. PCSELs are remarkable for their large-area, low-divergence emission ($< 1^\circ$) defined by a single or few optical modes. High-power PCSELs can achieve emission levels of several tens of watts, rivaling the best single high-power *edge-emitting* SLs. Modern PCSELs utilize PCs formed by periodic air voids in both lateral directions within the semiconductor material. As a part of the Leibniz Collaborative Excellence project PCSELence, we are collaborating with the Ferdinand Braun Institute (FBH) in Berlin to design a comparable PCSEL with an all-semiconductor PC layer. This innovation could significantly enhance both the efficiency and manufacturability of PCSELs.

Dynamic model, spectral problem, and numerical challenges

Model equations. The above-threshold behavior of PCSELs is described by a dynamic model based on three-dimensional coupled-wave theory. The field equations are represented by a system of four linear partial differential equations (PDEs) in one temporal and two spatial dimensions within the lateral domain $Q_{\mathrm{L}} = [0, L] \times [0, L]$:

$$\partial_t \Psi(x,y,t) = v_{\mathrm{g}}\Big[i(\mathbf{C} - \Delta\beta) - \begin{pmatrix} \sigma\partial_x & 0 \\ 0 & \sigma\partial_y \end{pmatrix}\Big]\Psi + \mathbf{F}_{\mathrm{sp}}, \quad (x,y) \in Q_{\mathrm{L}}, \quad \sigma \stackrel{\mathrm{def}}{=} \begin{pmatrix} 1 & 0 \\ 0 & -1 \end{pmatrix}. \tag{1}$$

These equations are derived using lateral Fourier expansions of the transverse-electric polarized field $\mathbf{E}(\mathbf{r}) = (E_x(\mathbf{r}), E_y(\mathbf{r}), 0)^T$ and the squared refractive index, $n^2(\mathbf{r}) = \sum_{\mathbf{s}\in\mathbb{Z}^2} \zeta_{\mathbf{s}}(z) e^{-i2\pi(s_1 x + s_2 y)/a}$, where a is the lattice constant of the PC. Four basic Fourier modes, $E_{y,(\pm1,0)}$ and $E_{x,(0,\pm1)}$, define the complex, slowly varying field amplitudes (Ψ_1, Ψ_2) and (Ψ_3, Ψ_4). These functions satisfy non-reflecting boundary conditions (BCs) at the edges of Q_{L} and form the vector function Ψ. L, v_{g}, $\Delta\beta$, $\mathbf{C}$, and $\mathbf{F}_{\mathrm{sp}}$ in (1) are the lateral size, group velocity, local change of the propagation factor, field coupling matrix, and stochastic spontaneous emission term, respectively [1]. In hot-cavity PCSELs, $\Delta\beta(x,y,t) = \frac{i}{2}[g - \alpha] + \Delta_n$ is a complex spatially distributed function. It accounts for the instantaneous local values of optical gain g, losses α, and refractive index-induced correction Δ_n, all of which depend on the local carrier density, governed by a diffusive carrier rate equation [1, 2]. More advanced models should also account for the gain dispersion, with additional

equations to model the frequency dependence of g and Δ_n [WIAS Preprint no. 809], self-heating effects, including three-dimensional heat transport equations for the entire PCSEL structure [WIAS Preprint no. 2558], and current spreading, defined by a three-dimensional Laplace equation with inhomogeneous BCs [WIAS Preprint no. 2421].

Construction of the field coupling matrix. The coupling of counter- and cross-propagating fields in (1) is realized through a complex (4×4) field coupling matrix, $\mathbf{C} = \mathbf{C}^{(1D)} + \mathbf{C}^{(RD)} + \mathbf{C}^{(2D)}$. The Hermitian submatrices $\mathbf{C}^{(1D)}$ and $\mathbf{C}^{(2D)}$ define one-dimensional coupling of basic waves and two-dimensional coupling from higher-order Fourier modes. The non-Hermitian $\mathbf{C}^{(RD)}$ represents the out-of-plane coupling to radiative waves, $E_{x,\mathbf{0}}$ and $E_{y,\mathbf{0}}$, determining laser emission. To define these matrices, we use i) the complex Fourier coefficients $\xi_{\mathbf{s}}(z)$ of the PC features (see, e.g., Figure 2(a)–(c)); ii) the vertical mode $\Theta(z)$ and respective effective refractive index (solid violet and black dashed lines in Figure 2(d), both defined by the vertical structure, red dots in the same panel); iii) the Green's functions $G_{\mathbf{s}}(z, z')$, which solve inhomogeneous Helmholtz problems and represent Fourier modes $E_{x,\mathbf{s}}$ and $E_{y,\mathbf{s}}$.

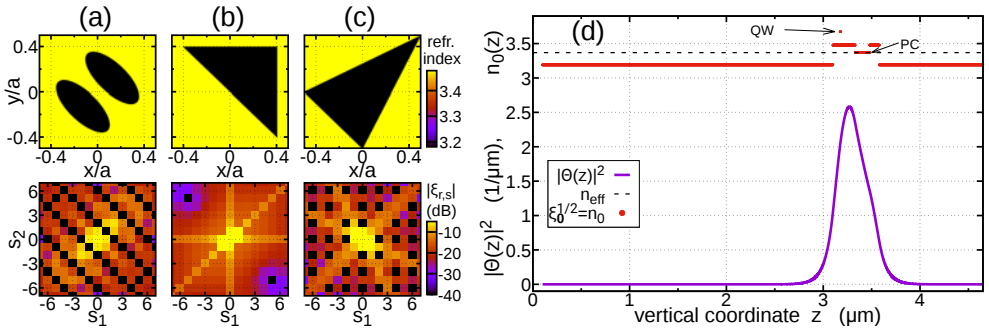

Fig. 2: *Defining structure of PCSELs. (a)–(c): Refractive indices within a unit PC cell (top) and $|\xi_{\mathbf{s}}|$ of leading Fourier coefficients (bottom). (d): Laterally-averaged (red) and effective (black dashed) refractive index, and vertical mode intensity (violet) along the vertical direction.*

We cannot use fully numerical algorithms to construct the submatrix $\mathbf{C}^{(2D)}$ because integrating the rapidly growing/decaying parts of $G_{\mathbf{s}}$ with moderate $|\mathbf{s}| \approx 10$ requires very fine numerical meshes, leading to huge computational times. Fortunately, within vertical layers, $G_{\mathbf{s}}$ and Θ can be represented by exponentials, allowing all required integrals to be solved analytically. However, direct use of analytic formulas can cause large- and small-number-related arithmetic issues, even at moderate $|\mathbf{s}| \approx 25$, and more so at ≈ 200. After resolving these problems [3], we can construct $\mathbf{C}$ for typical PCSELs using Fourier modes with $|\mathbf{s}| \leq 500$ in just a few seconds.

Spectral problem. The substitution of $\Psi = \Theta(x, y)e^{i\Omega t}$ into (1) yields the spectral problem

$$\begin{pmatrix} \sigma\partial_x & 0 \\ 0 & \sigma\partial_y \end{pmatrix}\Theta(x, y) = i[\mathbf{C} - (\Delta\beta + \tfrac{\Omega}{v_g})]\Theta, \quad (x, y) \in Q_L, \quad \textbf{+ BCs}. \tag{2}$$

For cold-cavity PCSELs with vanishing $\Delta\beta$, the imaginary and real parts of complex eigenfrequencies, $\Im\Omega$ and $\Re\Omega$, respectively, provide key information on the optical gain needed to excite the corresponding mode and its relative frequency. The enhanced threshold gain separation $\frac{2\Im(\Omega_1 - \Omega_0)}{v_g}$ between the fundamental mode with smallest $\Im\Omega$ and the first higher-order mode (second smallest $\Im\Omega$) suggests potential single-mode operation in well pumped (hot-cavity) PCSELs. In contrast to the spectral problems in narrow-waveguide edge-emitting lasers [WIAS Preprint no. 939], exact

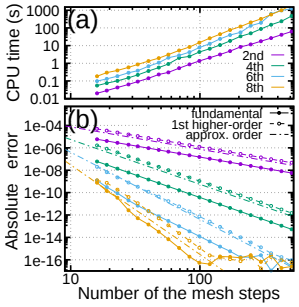

Fig. 3: *CPU time (a) and main mode precision (b) as functions of the mesh step number for various precision order schemes*

solutions of (2) are not available. To approximate the most important modes, we replace the continuous problem with a finite difference scheme [3]. In [3, 4, 5], we showed that relatively coarse numerical meshes and simple second-precision-order schemes can provide good approximations of the most important eigenfrequencies. Precision can be improved by using higher-order precision schemes and/or refining the meshes for a few selected modes, as shown in Figure 3 and [3].

Tailoring all-semiconductor PCSELs

Compared to the air-void-based PCs in modern PCSELs, all-semiconductor PCs have a lower refractive index contrast. This results in relatively weak field coupling terms in $\mathbf{C}$, meaning light generation requires larger PC features and PCSELs ($L \geq 1$ mm). Additionally, due to technological challenges, well separated features are preferred. Therefore, instead of dual lattice configurations like in Figure 2(a), simpler large triangle PC features are favored, as shown in Figure 2(b) and (c).

PCs with isosceles triangular features. Using diagonally-symmetric features, as shown in Figure 2(a)–(c), simplifies the matrix $\mathbf{C}$ and leads to analytic expressions for its eigenvalues $\Omega_{\mathbf{C}}$. In particular, all $\Im\Omega_{\mathbf{C}}$ are defined by combinations of only a few entries of the coupling matrices, specifically $\Im\mathbf{C}_{1,1}^{(\mathrm{RD})}$ and $[\mathbf{C}_{1,2} \pm \mathbf{C}_{1,4}^{(\mathrm{2D})}]e^{-i\,2\arg\xi_{(1,0)}}$. $\Omega_{\mathbf{C}}$ serve as accumulation points for the eigenfrequencies Ω in large cold-cavity PCSELs, providing an approximation for the gain of the fundamental mode. Thus, when designing PC features, we should aim for large $|\xi_{(1,0)}|^2$ (a prefactor of $\mathbf{C}^{(\mathrm{RD})}$) and adjust $\arg\xi_{(1,0)}$. Additionally, to prevent the dominance of $\mathbf{C}_{1,2}^{(\mathrm{1D})}$ in the overall one-dimensional coupling factor $\mathbf{C}_{1,2}$, $\xi_{(2,0)}$ (a prefactor of $\mathbf{C}^{(\mathrm{1D})}$) should be kept small. Isosceles triangles, characterized by the length b and the height h along the diagonal of the unit cell, are the simplest nontrivial diagonally-symmetric features. The factors $\xi_{(1,0)}$ and $\xi_{(2,0)}$ for these features can be expressed as analytic functions of b and h, as shown in Figure 4, where $|\xi_{(2,0)}(b,h)|$ is plotted. The dashed line represents right isosceles triangles (RIT), considered in early works on small PCSELs with air-void-based PCs. Regions above and below this line correspond to acute and obtuse triangles, while the empty region in the upper right corner indicates large triangles that overlap with neighboring PC features. The white box in the diagram represents an RIT with a side length of $0.8a$, as shown in Figure 2(b). Among other RITs, it exhibited the most desirable $L = 0.8$ mm-PCSEL characteristics at the lasing threshold [1]. The white triangle in Figure 4 marks a special stretched isosceles triangle (SIT) from Figure 2(c), where $\xi_{(2,0)}$ vanishes. This makes PCs with this SIT comparable to dual-lattice PCs, as seen in the lower panels of Figure 2(a) and (c).

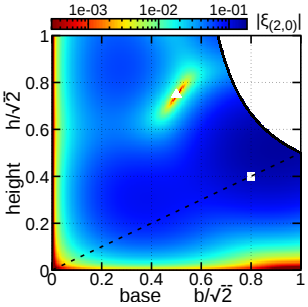

Fig. 4: *Factors $|\xi_{(2,0)}|$ in all non-overlapping isosceles triangles. Dashed: RITs. White box and triangle: Cases shown in Figure 2(b) and (c).*

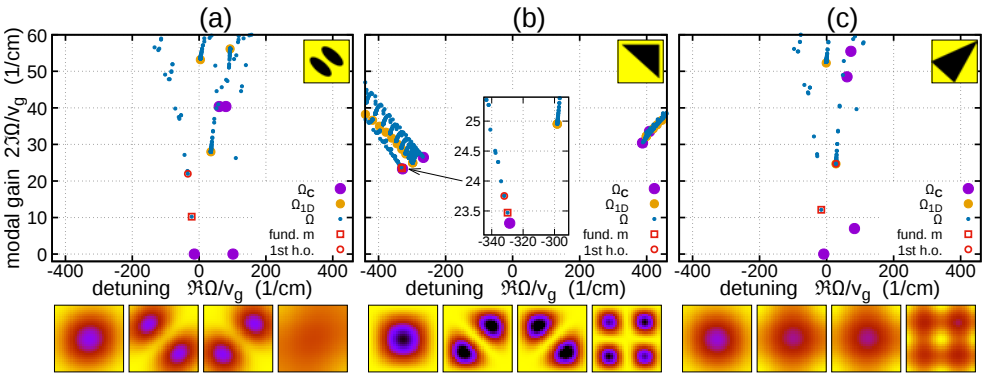

Fig. 5: *Mode calculations for three $L = 1$ mm PCSELs defined in Figure 2. Top: Eigenfrequencies Ω (blue), 1D modes in the decoupled system (orange), and $\Omega_{\mathbf{C}}$ (violet). Red box and circle: The fundamental and 1st higher-order modes. Bottom: Intensity distributions $|\Theta(x,y)|^2$ for four main modes in each case.*

Cold-cavity PCSELs. In Figure 5, mode calculations are shown for three cold-cavity $L = 1$mm-PCSELs from Figure 2. For the optimized RIT-PC-based PCSEL (panel b), four violet bullets $\Omega_{\mathbf{C}}$ and orange bullets $\Omega_{1\mathrm{D}}$ (one-dimensional modes of (2) with neglected cross-propagating field coupling [3, 5]) act as accumulation points for eigenfrequencies Ω (blue dots). Similar modal gain values suggest multimode operation of the well-biased PCSELs. In contrast, dual-lattice-PC-based (a) and special SIT-PC-based (c) PCSELs exhibit large threshold gain separation between two main modes (red circle and box), predicting single-mode operation with strong side-mode suppression in hot-cavity PCSELs. Both of these configurations have their drawbacks. First, the imaginary part of the leading $\Omega_{\mathbf{C}0}$ is almost zero in both cases, leading to weak vertically outcoupled and emitted field intensity. The desired increase of $\Im\Omega_{\mathbf{C}0}$ can be achieved by introducing deviations from the ideal dual-lattice or special SIT [2, 6] configurations. Second, the large separation between the fundamental Ω_0 and the leading $\Omega_{\mathbf{C}}$ results in significant field leakage through the lateral borders, weakening the fields in the central part of the PC domain. This flattening of mode intensity is evident in the lower panels of Figure 5(a) and (c), compared to (b). Field leakage can be mitigated (at the cost of reduced modal gain gap) by increasing the lateral size L of the device.

Dynamic simulations. In all examples above, we considered modes in cold-cavity PCSELs. This means that discussions on single-mode lasing and side-mode suppression apply mainly near the lasing threshold, where the propagation factor $\Delta\beta$ in (1) and (2) remains spatially uniform. However, at high-power regimes, spatial hole burning of carriers, inhomogeneous pumping, and self-heating cause $\Delta\beta(x, y)$ to become non-uniform. This leads to significant changes in the calculated eigenfrequency landscape. To determine if single-mode lasing is achievable, we performed transient simulations using the full dynamic model for PCSELs.

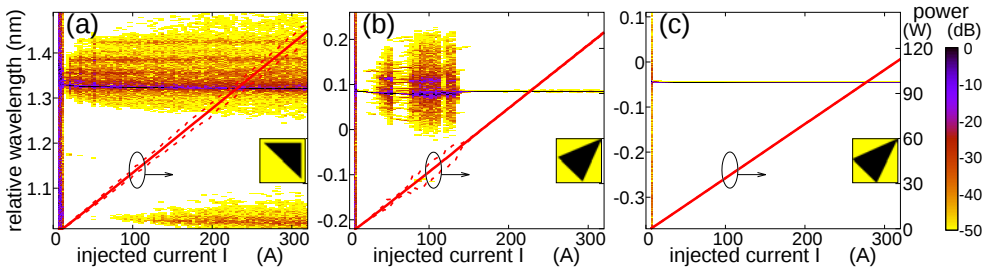

Fig. 6: *Optical spectra (color maps) and emitted power (red lines) for $L = 2$mm PCSELs as functions of up-tuned bias current. Panels (a), (b), and (c) depict PCSELs with RIT- and two different SIT-based PCs.*

In Figure 6, we present simulations of three $L = 2$mm-PCSELs with an optimal RIT-based and slightly differing SIT-based PC layers. The vertical laser structure is defined in Figure 2(d) and [1]. Due to the small threshold gain separation in the cold-cavity device, the RIT-based laser (panel a) demonstrates multimode emission for all bias currents. In contrast, both SIT-based lasers exhibit the desired single-mode lasing. In case (b), where multimode lasing occurs within a limited bias current range, the SIT choice was made to increase emitted power (i.e., increase $\Im\Omega_0$) while maintaining a decent mode threshold gap in the cold-cavity laser. The emission power from this device is comparable to that of the optimized RIT-based laser. On the other hand, SIT features in case (c), also discussed in [6], were selected to improve side-mode suppression, but resulted in a reduced $\Im\Omega_0$. Consequently, our dynamic simulations show perfect single mode emission across the entire bias current range, with a slight decrease in emission power. These results give us confidence

that achieving single-mode lasing in large-area all-semiconductor PCSELs with SIT-based PCs is possible.

Conclusions and outlook

In conclusion, we developed a numerical tool capable of efficiently constructing and solving the spectral problem for PCSELs [3, 4, 5]. Simulations and analysis of the field coupling matrix and calculated spectra led us to identify a special large SIT PC feature [6]. This configuration shares properties with conventional dual-lattice features used in modern air-void-based PCSELs and may be advantageous when designing all-semiconductor devices. A patent application for the use of SIT features in PCSELs has been submitted to the German Patent Office. Further improvements in PCSELs can be achieved by integrating the Bragg grating layers, tuning their separation from the active layer [6], modifying the vertical structure, or using alternative, more complex features with properties similar to those of the above considered SITs. Our first dynamic simulations [2] predict that large ($L \geq 2$mm) PCSELs with SIT-based all-semiconductor PCs should maintain good side-mode suppression. In contrast to our earlier work with RIT-based PCSELs [1], these should demonstrate the desired single-mode emission. Further simulations, using advanced models accounting for self-heating in PCSELs, will be conducted later within the PCSELence project. It remains to be seen whether the all-semiconductor PCSELs being built at the FBH will demonstrate the expected single-mode emission.

References

[1] H. Wenzel, E. Kuhn, B. King, P. Crump, M. Radziunas, *Theory of the linewidth-power product of photonic-crystal surface-emitting lasers*, IEEE J. Quantum Electron., **61** (2025), pp. 2400114/1–2400114/14.

[2] M. Radziunas, H. Wenzel, B. King, P. Crump, E. Kuhn, *Dynamical simulations of single-mode lasing in large-area all-semiconductor PCSELs*, Opt. Lett., **50** (2025), pp. 1953–1956.

[3] M. Radziunas, E. Kuhn, H. Wenzel, *Solving a spectral problem for large-area photonic crystal surface-emitting lasers*, Math. Model. Anal., **29** (2024), pp. 575–599.

[4] M. Radziunas, E. Kuhn, H. Wenzel, B. King, P. Crump, *Calculation of optical modes in large emission area photonic crystal surface-emitting lasers*, in: 23rd International Conference on Numerical Simulation of Optoelectronic Devices (NUSOD) 2023, P. Bardella, A. Tibaldi, eds., IEEE 2023, pp. 89–90.

[5] M. Radziunas, E. Kuhn, H. Wenzel, B. King, P. Crump, *Optical mode calculation in large-area photonic crystal surface-emitting lasers*, IEEE Photon. J., **16** (2024), pp. 0601209/1–0601209/9.

[6] B. King, H. Wenzel, E. Kuhn, M. Radziunas, P. Crump, *Design of very-large area photonic crystal surface emitting lasers with an all-semiconductor photonic crystal*, Opt. Express, **32** (2024), pp. 44945–44957.